Effect of argon and nitrogen atmospheres on the properties of stainless steel 316 L parts produced by laser-powder bed fusion

Materials and Design 179 (2019) 107873

Contents lists available at ScienceDirect

Materials and Design

journal homepage: www.elsevier.com/locate/matdes

Effect of argon and nitrogen atmospheres on the properties of stainless steel 316 L parts produced by laser-powder bed fusion

Camille Pauzon [a,*], Eduard Hryha [a], Pierre Forêt [b], Lars Nyborg [a]

[a] Department of Industrial and Materials Science, Chalmers University of Technology, SE-412 96 Göteborg, Sweden
[b] Linde AG AT EMEA, Carl-von-Linde-Straße 25, DE-85 716 Unterschleißheim, Germany

HIGHLIGHTS

- Gas monitoring system allows to lower and keep oxygen on the level of tens of ppm
- Gas type and purity, L-PBF hardware and alloy type determine pick-up of oxygen and nitrogen
- 316 L is a robust material whose chemistry and properties are not affected by O_2 levels between 20 and 1000 ppm
- Only slightly higher nitrogen pick-up of about 50 ppm is observed when N_2 is used in L-PBF
- Atmosphere of lower purity result in early powder degradation

GRAPHICAL ABSTRACT

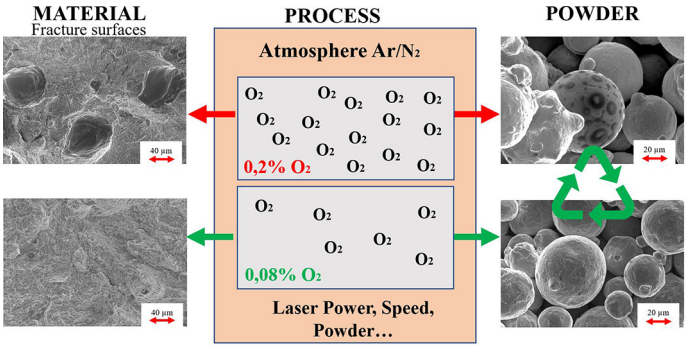

ARTICLE INFO

Article history:
Received 3 March 2019
Received in revised form 21 April 2019
Accepted 16 May 2019
Available online 17 May 2019

Keywords:
Additive manufacturing
Laser powder bed fusion
316 L austenitic stainless steel
Argon
Nitrogen
Atmosphere purity
Surface chemistry
Mechanical properties

ABSTRACT

The role of the inert gas during laser powder bed fusion (L-PBF) is to remove the process by-products and the air that is initially present in the process chamber. On this purpose, different gas supply options are available. The effect of the process gas and its purity, using argon and nitrogen, on the properties of the 316 L stainless steel produced by L-PBF was studied. The results obtained showed that utilization of argon and nitrogen result in residual oxygen levels that vary over the course of the process sequence in the process chamber. It can be concluded that 316 L stainless steel is a robust alloy to process by L-PBF. A limited effect of the residual oxygen or the gas type (argon or nitrogen) on the tensile properties of the 316 L stainless steel parts was registered. The oxygen and nitrogen pick-up within the produced parts are limited. However, when processing 316 L stainless steel with lower purity gas supply such as a nitrogen generator, risks related to powder degradation arise. Out of the available gas options, the findings highlighted that processing with high purity argon ensures limited powder degradation and high toughness of the produced parts.

1. Introduction

The industrial success of the laser powder bed fusion (L-PBF) process is driven by the development of robust production parameters. These cover from the laser, scanning and process chamber parameters to the metal powder specification, through the definition of the design rules.

* Corresponding author.
E-mail address: pauzon@chalmers.se (C. Pauzon).

https://doi.org/10.1016/j.matdes.2019.107873

The 316 L stainless steel has been thoroughly investigated as the most robust and applied material in metal additive manufacturing (AM). Significant efforts have been put in understanding how the laser energy input affects the produced parts properties in terms of porosity, microstructure and mechanical properties. Zhong et al. [1] showed that the high yield strength of 316 L stainless steel built by L-PBF can be correlated to its very fine hierarchical microstructure consisting of macro-, micro- and nano-structures. This microstructure consists of several melt pool boundaries revealed upon etching, and large columnar grains aligned along the building direction containing several of these melt pools [2]. Within the grains, a cellular microstructure is usually obtained and attributed to the high cooling rates involved during the L-PBF process. The cell boundaries have proven to be preferential sites for segregation of Cr and Mo and limit the movement of dislocations [3]. As a result, the strength of the produced material is comparable or even better than that obtained by conventional means such as casting. Besides, the as-built material is characterized by some anisotropy in properties. Casati et al. [4] studied in detail the effect of the anisotropy of the built 316 L material on its mechanical properties and failure behaviour. They stressed that the early failure of vertically built samples can be attributed to the distribution of defects such as partially molten powder particles. Cherry et al. [5] focused on the effect of the laser exposure time on the density, microstructure and hardness of 316 L stainless steel built by L-PBF. They showed that the laser energy density affects the melting behaviour. They noted convex surface features, also referred to as balling, upon low energy inputs. Sun et al. [6] investigated the use of high laser scanning speeds to achieve high density 316 L parts and thus, increase the overall build rate. Finally, Riemer et al. [7] showed that 316 L material produced by L-PBF exhibits fatigue properties similar to that of conventionally produced material.

Still, the importance of the process gas, and process parameters connected to it are seldom addressed. As a result, the scope of the process gases used for L-PBF is limited to the inert argon and nitrogen. Argon is a noble gas, while nitrogen is a molecule that can dissociate. Nitrogen atoms can then react with other species like oxygen, hydrogen and sulphur. They may also dissolve in the molten metal as well as form nitrides with active metals, *e.g.* chrome, titanium, vanadium, *etc.*

The main role of the process gas is protection from oxidation. When the powder bed interacts with the laser beam, its temperature increases significantly, and the formation of stable oxides is likely to occur. To protect the material from oxidation, the required atmosphere purity is generally established by flushing the process chamber volume with the selected gas. The flushed gas is then vented out. The oxygen and impurities initially present in the chamber are diluted - but not necessary minimized to the thermodynamically required level. This continues until the machine detects less than a given oxygen level and starts to recirculate the gas. Machine manufacturers do propose alternatives to establish the required process atmosphere composition and purity, typically utilizing extensive flushing. Another solution is to first evacuate the entire chamber, creating a low vacuum and then back flushing with inert gas ([8]. This may be repeated several times to achieve the required atmosphere before the process starts.

The directed gas flow also enables the removal of process by-products, helping to limit any further interaction between them and the laser beam. The generation of these projections has been tackled by simulation and by *in-situ* observation of the melt pool. Matthews et al. [9] highlighted the presence of a denudation region close to the laser tracks where the metal particles are removed. They studied the evolution of the denudation for different laser parameters and ambient pressures. Khairallah et al. [10] also explained the denudation phenomenon. It has been shown that the surface tension of the melt pool may vary because of some surface-active elements, as well as the temperature gradient. As the surface tension decreases with increasing temperature, the liquid flows from the centre of the melt pool to the edges, *i.e.* from low surface tension areas to the high surface tension areas. This is the so-called Marangoni effect. If the latter is significant, the melt pool may become unstable and material may be ejected from it. The thermal conductivity of the gas can affect the temperature gradient and thus the Marangoni effect. In addition, the melt pool temperature can locally overcome the vaporization temperature. The latter decreases with decreasing atmosphere pressure [11]. If so, an evaporation flow takes place, *i.e.* a vapour jet [12]. The metal vapour expands against the ambient gas [13]. The vapours may condense into fumes by combining with oxygen. Different metal ejections can take place because of the evaporation flow. Ly et al. [14] classified them as follows: i) some particles are entrained by the gas flow and can be pulled into the melt pool, adding up to it; ii) some particles can travel through the vapour jet but not the laser beam, *i.e.* “cold particles”; iii) others can travel through the vapour jet and intersect the laser beam, *i.e.* “hot particles”.

Ladewig et al. *[15]* suggested that a low gas flow velocity promotes the redeposition of these by-products. The authors noted that balling is also more likely observed in this regime, resulting in lack-of-fusion defects, and increased porosity. Balling may also be promoted by the residual oxygen in the atmosphere, as shown by Li et al. [16] that above 1000 ppm O_2 the wettability of the liquid metal with the previously deposited and oxidized material is worsened, leading to significant ball formation. Besides, Ferrar et al. [17] also highlighted the importance of the gas flow uniformity to achieve low porosity independent from the position of the part on the building platform.

There are numerous studies published focusing on the melt pool dynamics and the effect of the gas flow on the parts quality ([14,18,19]. However, the role of the gas composition and purity in the interaction with the laser and the powder is still not understood.

This study aims at understanding the gas - metal powder interaction during the L-PBF process and to comprehend the capabilities of actual systems regarding the available gas options for 316 L austenitic stainless steel. Deeper insight is given on the effect of the typically used gases (and their purity levels) on the properties of the produced parts in terms of chemistry, microstructure and mechanical properties.

2. Experimental procedures

The 316 L stainless steel specimens were produced using standard gas atomized powder and an *EOS M290* (*EOS GmbH*) machine that is equipped with a Yb-fibre laser of maximal nominal power 400 W. The particle size distribution was determined using a *CAMSIZER X2* and was found to be between 20 and 53 μm. A powder layer thickness of 20 μm and the standard process parameters for 316 L stainless steel developed by *EOS GmbH* for the *M290* machine, were used.

This study compares different process atmospheres that were distinguished between standard and controlled ones. The standard conditions are the process atmospheres that are available to any *EOS M290* user. Under such circumstances, the residual oxygen within the chamber is a result of the machine characteristics: the flushing time, the gas flow, the gas recirculation, the humidity within the chamber, the leak rate, *etc.* The machine operates so that the oxygen level does not overpass a threshold value. The oxygen level is analysed by oxygen sensors at the top of the process chamber and in the recirculation system. In this study, standard conditions were established using Argon 5.0, Nitrogen 5.0 and the nitrogen produced by the internal generator, see Table 1.

During the operation of an *EOS M290* machine, the initial atmosphere is diluted by the process gas during the flushing of the chamber.

Table 1
Gases considered in this study.

Gases	Purity	Process O_2 threshold
Argon 5.0	≥99.999%	1000 ppm
Nitrogen 5.0	≥99.999%	1000 ppm
Nitrogen from the internal generator	Could be from 95% to 99.5%	10,000 ppm

When the measured oxygen level is below 10,000 ppm, the gas is recirculated. An additional holding gas flow makes it possible to achieve a lower oxygen level and compensates for the possible leakages of the system. When the machine sensors measure an oxygen level of 1000 ppm or less, the process starts. Some machine manufacturers also integrate a nitrogen generator into their machine. The generator permits the production of nitrogen from compressed air. When using it, operating conditions are slightly changed. The gas recirculation will start earlier, and the process will be launched when 10,000 ppm of O_2 is detected. The three different processing conditions described above result in vastly varying partial pressure of the gas components. In addition, because the initial atmosphere is diluted, a significant fraction of nitrogen and impurities will remain (in proportion to the initial oxygen fraction).

On one hand, Argon 5.0 and Nitrogen 5.0 contain less than 10 ppm of impurities (*i.e.* water, oxygen, and nitrogen). On the other hand, the internal nitrogen generator inside the *EOS M290* uses gas separation membranes. The membrane consists of a bundle of hundreds or thousands of polymer hollow fibres. The air is fed into one end of the hollow fibres. Water vapour, carbon dioxide and oxygen have a higher permeation rate than nitrogen and argon, due to their smaller molecular size; meaning that they will more rapidly diffuse within the fibre walls and be vented out. Along the fibres, the air gets richer in nitrogen. The typical purity of the produced nitrogen varies between 95% (*i.e.* 50,000 ppm impurities) and 99.5% (*i.e.* 5000 ppm impurities). The membrane lifetime can be controlled thanks to purity gauges but it still degrades over time.

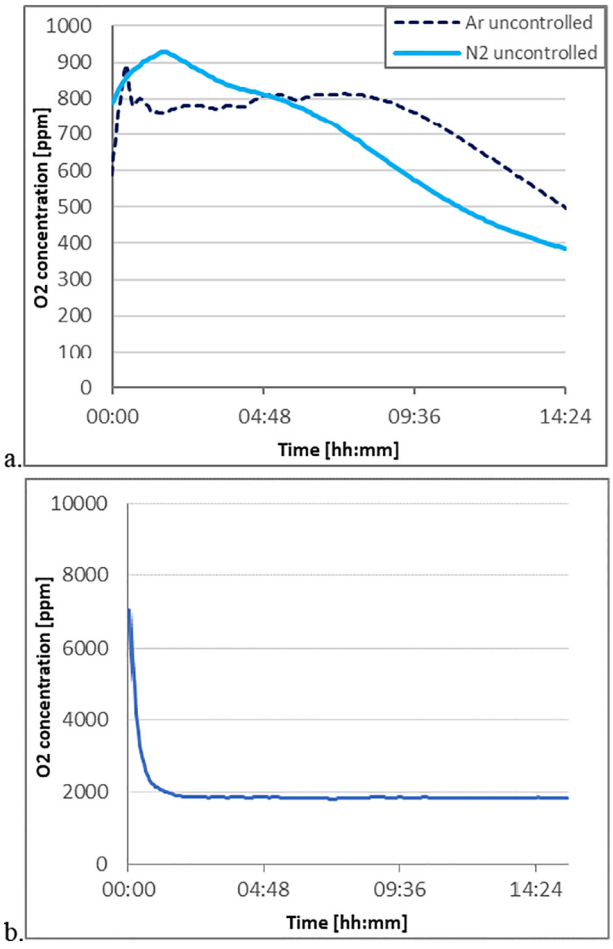

Fig. 1. O_2 content analysed for uncontrolled conditions: a. in Argon 5.0 and Nitrogen 5.0, b. using the nitrogen generator.

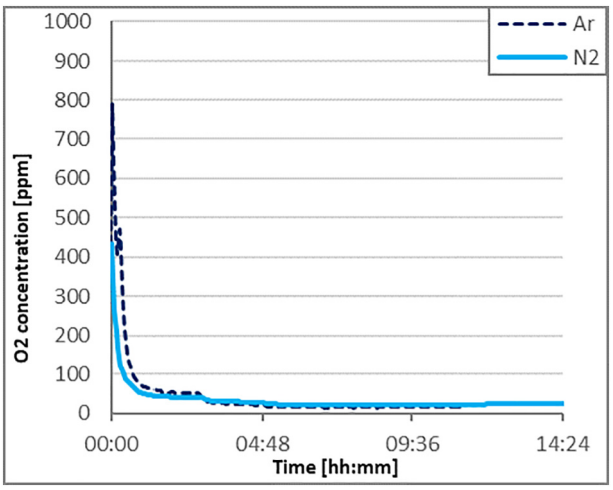

Fig. 2. O_2 content monitored at 20 ppm O_2 in argon and nitrogen.

The controlled conditions during the processing of the samples were achieved using an external oxygen monitoring device, the *ADDvanceO2® precision* (*Linde Gas*). This system is attached to the *EOS M290* machine and samples 1 L of gas every minute at a location near the powder bed. This gas sample is analysed by an oxygen sensor and then brought back to the machine. The sensor is an electrochemical cell consisting of an anode, an electrolyte and a cathode. Oxygen molecules are reduced at the cathode while the anode made of lead is oxidized. The measured oxygen level is proportional to the rate at which oxygen molecules reach the cathode. The system is calibrated with calibration gases (argon and nitrogen) of very accurate concentration (± 1 ppm O_2) prior to using. The operator may also define an oxygen set point to be achieved within the process chamber. The oxygen level in the chamber is adjusted accordingly, depending on the measured value. In this study, the *ADDvanceO2® precision* was used to analyse the oxygen level in the standard conditions. It was also employed to compare the use of argon and nitrogen at different oxygen levels, *i.e.* 20 ppm O_2 and 800 ppm O_2, respectively. The system offers the opportunity to measure the oxygen content close to the interaction area and is not cross sensitive to species like hydrogen. It also permits to measure the humidity of the gas sample (*i.e.* dew point).

To compare the parts produced under different atmospheres, a standard build job was developed. For this standard build job, test bars were printed: 5 net-shape tensile specimens according to ISO 2740 and tested

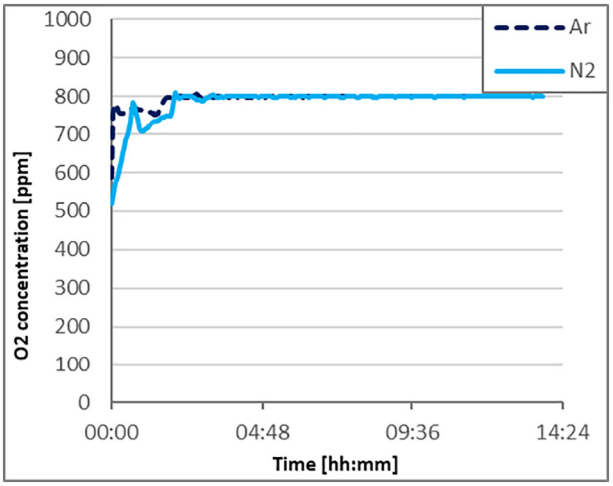

Fig. 3. O_2 content monitored at 800 ppm O2 in argon and nitrogen.

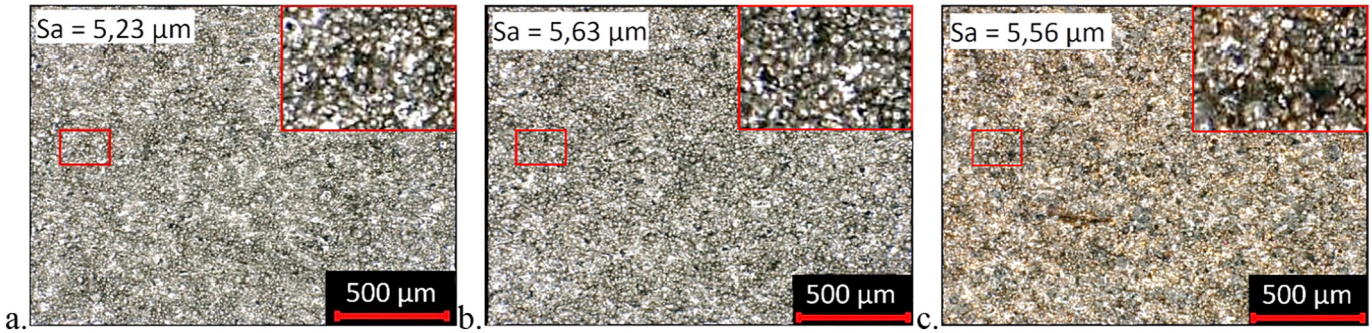

Fig. 4. Side surface roughness under a. Uncontrolled argon, b. Uncontrolled nitrogen and c. Nitrogen from the generator.

according to the standard NF EN 10002-1, 5 net-shape impact specimens (55 × 10 × 10 mm^3) according to ISO 5754 and 3 cubes (15 × 15 × 10 mm^3). The surface roughness of the cubes was analysed using a *Keyence VHX-6000 series* numerical microscope. The produced cubes were mounted, ground, and polished following *Struers* metallographic procedure. The relative porosity of the cubes was measured using the digital microscope and a stitching option allowing to reconstruct an overview image of the cross section from pictures taken at high magnification (×500). Finally, the polished sections were electro-etched in a 10% oxalic acid solution. The powder morphology as well as the microstructure and the fracture surface of the produced samples were investigated using the high-resolution scanning electron microscope (HR-SEM), *LEO Gemini 1550* equipped with a secondary electron in-lens detector offering enhanced lateral resolution. The qualitative evaluation of the composition of inclusions observed during SEM analysis was determined by means of energy dispersive X-ray spectrometry (EDX) with *INCA X-sight*. The powder and components chemistry were measured by carrier gas hot extraction (CGHE) for oxygen, hydrogen and nitrogen using a *LECO ONH836*, and inductively coupled plasma optical emission spectroscopy (ICP-OES) for carbon and sulphur using a *SPECTRO ARCOS*.

The last set of analysis dealt with powder sampling. The goal of this inspection was to highlight possible differences in degradation rates under each standard processing condition. To do so, powder samples were collected for the standard argon atmosphere and for the lower purity nitrogen, to be studied using the HR-SEM. The particles were taken once the previously described build jobs were completed. Powder samples were picked-up near the parts (less than 1 cm away from the parts' edges with a spoon) after three cycles under uncontrolled Argon 5.0 and one cycle under nitrogen from the generator. The virgin powder was also sampled and taken as a reference. The powder particles were gently pressed between aluminum plates which were set on a SEM sample holder later on.

The software HSC Chemistry 9 (Outotec Research Oy, Pori, Finland) was used to perform calculations of the thermodynamic stability of oxides.

3. Results and discussions

3.1. Oxygen levels

3.1.1. Standard atmospheres

Fig. 1 displays the analysed oxygen levels when the L-PBF machine is running in standard conditions. The job is started as soon as the machine detects 1000 ppm O_2 for technical gases and 10,000 ppm O_2 for the nitrogen generator. This corresponds to time zero in Fig. 1 a and b.

Under argon, the average oxygen level of the standard job is 731 ± 98 ppm O_2 and the dew point is −27 ± 1 °C. Under nitrogen, the oxygen level is 656 ± 191 ppm O_2 and the dew point is −31 ± 1 °C. The variation between both gases may be explained by the presence of individual gas lines for each gas. Indeed, they may have different leak rates. For both argon and nitrogen, a peak is observed after the process started, after 1 h for argon and 2 h for nitrogen. This could be explained based on the fact that the flushing gas flow rate is more important than the holding gas flow rate, or because of the machine leaks. It could be that the connections for the argon flow are less tight than the ones for the nitrogen flow, thus the earlier peak for argon. Later, under argon, the oxygen level is relatively stable and drops after 8 h. Under nitrogen, the oxygen is reduced to 400 ppm O_2. This drop could be explained by a progressive elimination of the impurities by the gas recirculation and the holding gas flow.

When using the internal generator to produce nitrogen, the oxygen level measured is 1985 ± 172 ppm O_2 and the dew point is −43 ± 2 °C. As observed in Fig. 1b, the oxygen level drops significantly during the first hour, from about 7000 ppm to 1900 ppm O_2. This time lap corresponds to the support generation of the parts. Therefore, the oxygen content is stable while the functional parts are being built. Afterwards, the oxygen level is more stable than under Argon 5.0 or Nitrogen 5.0, although the value is higher. Besides, the atmosphere is drier than for the other standard and controlled conditions. This might be explained because the produced gas flow from the generator is influenced by the incoming air flow. While incoming technical gas pressure is set to about 5 bars, the compressed air pressure has to be at least 10 bars so that the

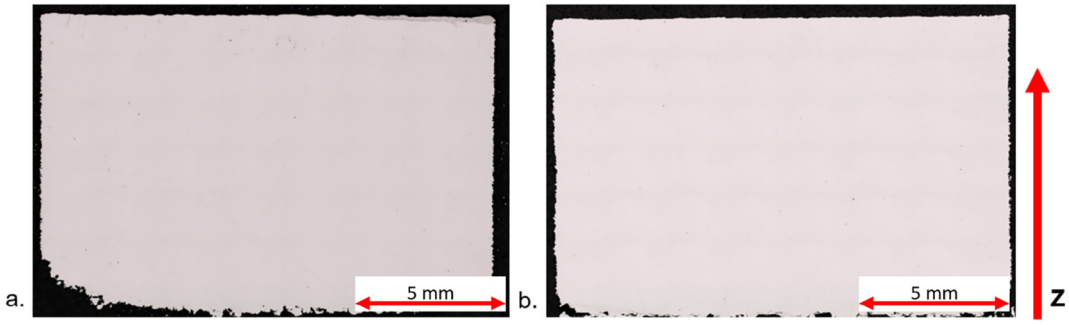

Fig. 5. Example of polished cross sections used for porosity determination: a. Argon at 800 ppm O2 and b. Internal nitrogen generator.

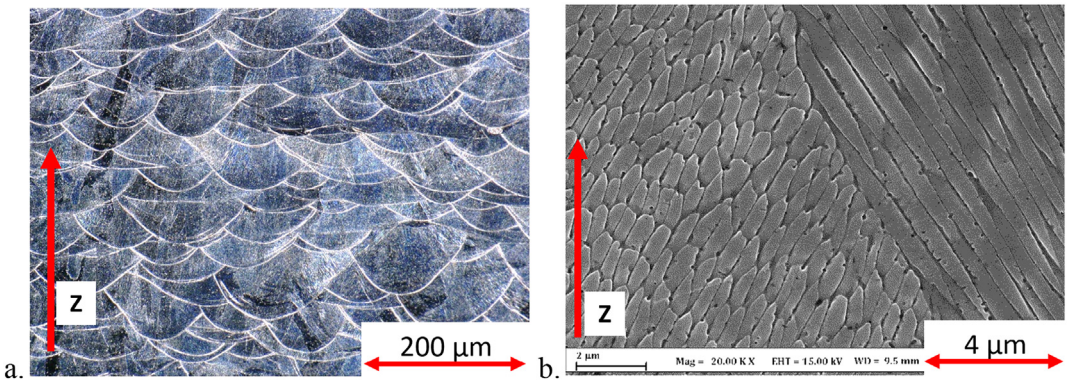

Fig. 6. Microstructure of the cross section of a cube produced under controlled argon observed with a. light microscope and b. HR SEM.

generator functions properly. Therefore, it is likely that the holding flow using the generator is higher than when using technical gases. A higher holding flow is also consistent with better dilution of impurities and thus lower dew point. Besides, the nitrogen generator is likely to feature a dryer, to remove the humidity of the compressed air, ensuring a dry nitrogen supply.

3.1.2. Controlled atmosphere

Fig. 2 and Fig. 3 display the recorded oxygen levels within the chamber at 20 ppm O_2 and 800 ppm O_2, during the establishment of the process conditions and during the built. The oxygen monitoring is started before each build job and the oxygen control starts at the time zero. To achieve a stable high residual oxygen level, it has been necessary to manually shut down the holding gas flow before starting the process. The process is manually initiated when the oxygen level is stable, after about 1 h. The oxygen level may still vary slightly during the first layers of the built which corresponds to the support generation. Under nitrogen, the average oxygen content and dew points of the builds were: 23 ± 3 ppm O_2 and -51 ± 2 °C; and 794 ± 19 ppm O_2 and -28 ± 1 °C. Under argon, it was: 24 ± 14 ppm O_2 and -46 ± 3 °C; and 795 ± 17 ppm O_2 and -22 ± 1 °C. The jobs were completed after 14 h 50 min. The control of the oxygen level is held over this time, see Fig. 2 and Fig. 3. The oxygen level variations are much reduced in comparison to the standard processing conditions (*cf.* Fig. 1), and the dew points are similar.

To achieve a low oxygen level within the chamber, fresher dry technical gas must be flushed in. It helps to dilute impurities such as oxygen but also reduce the humidity. When working at 800 ppm O_2, in conditions close to the standard one, the system does not need to be flushed with gas. Working at 20 ppm O_2, more gas is needed. Thus, the humidity is reduced and so is the dew point.

In addition, when 20 ppm of oxygen remains in the chamber, about 75 ppm of nitrogen must be considered. Similarly, when 800 ppm of oxygen remains, about 2980 ppm of nitrogen are also likely to be present.

3.2. Effect of process gas purity on roughness, density and microstructure

Fig. 4 shows the side of the cubes built under standard conditions. The roughness is not much affected by using the argon or nitrogen process gases. Similar side surface roughness was obtained for the material processed under controlled conditions. However, some discoloration is observed for the cube processed with the internal nitrogen generator, highlighting a pronounced oxidation of the surface.

No differences in the microstructure were observed between argon and nitrogen processed parts and all the parts achieved a relative density of $99.96 \pm 0.02\%$, see the cross section of the cubes in Fig. 5.

Fig. 6a shows the commonly observed microstructure for 316 L stainless steel parts produced by L-PBF along the building direction composed of several melt pool boundaries of light contrast [2]. As shown by several authors, columnar grains aligned with the building direction are passing through several of these melt pool boundaries ([1,4,20,21]. This is highlighting the epitaxial growth of grains nucleating on previously formed layers, along the steepest thermal gradient. Upon higher magnification, a fine cellular structure is noted within the grains, see Fig. 6b.

3.3. Effect of process gas purity on the sample chemistry and mechanical properties

Fig. 7 and Fig. 8 highlight the C, O, N, S, and H content in the material produced in controlled argon and nitrogen. The chemical analysis is performed on the bulk part of the produced components. The content of O, N and H in the virgin powder is also displayed. Nitrogen pick-up occurs through diffusion and thus the absorption rate is limited by the presence of nitrides or oxides within the material, *i.e.* at the melt pool surface, powder surface and solidified material surface. Working at lower oxygen levels implies a reduced dew point which may enhance the absorption of nitrogen by removing/minimizing surface oxides.

Still, under controlled argon, the chemistry of the sample does not change significantly for different residual oxygen levels. This may be explained by the fact that even though the dew point is low for the 20 ppm O_2 condition, the residual nitrogen which may be absorbed is much lower than at 800 ppm O_2. Under nitrogen, since the nitrogen partial pressure is higher, the nitrogen solubility increases. About 50 ppm more nitrogen is measured in comparison to samples processed under argon. For lower oxygen level, the low dew point does not enhance the nitrogen absorption. Besides, the oxygen pick-up does not decrease for lower oxygen levels neither in argon nor in nitrogen. The

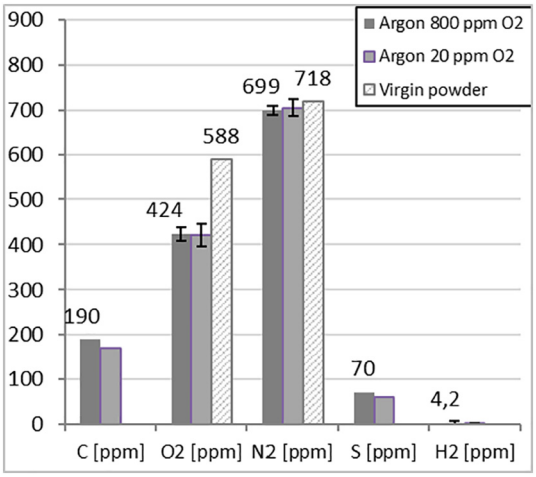

Fig. 7. Chemical analysis of built parts in argon.

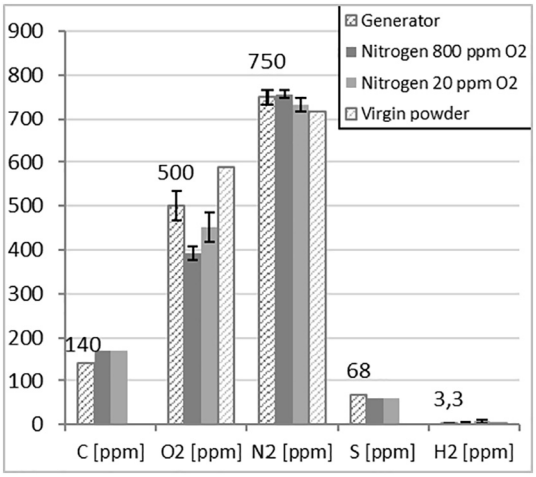

Fig. 8. Chemical analysis of built parts in nitrogen.

concentrations of carbon and sulphur in the compacts are not significantly affected by the atmosphere purity.

It seems that most of the nitrogen is transferred from the powder to the part, while there is an important loss of oxygen. The initial oxygen content in the powder and in the chamber atmosphere must balance the oxygen content in the remaining powder, in the produced parts, in the metal projections and in the atmosphere (*i.e.* fresh and recirculated gas, and gas leaks). It could be that the oxide covering the powder particle surface is exposed to the laser radiation and dissociates. The produced oxygen gas is further removed by the gas flow. In addition, the oxygen loss is partly balanced by an oxygen pick-up by the process by-products and spatter projections. The study of the oxidation state of these particles is not covered in this work. The powder bed also constitutes a potential gettering material in comparison to the built material.

The chemical analysis of the parts produced in the different nitrogen atmospheres shows that the lower residual oxygen control enables to significantly reduce the oxygen pick-up and a little bit the nitrogen pick-up, see Fig. 8. The highest oxygen pick-up is observed for the material produced using the internal nitrogen generator. It is about 100 ppm O2 higher than when using technical gases in standard or controlled conditions. This is consistent with the much higher residual oxygen remaining in the chamber, see Fig. 1. Still, the nitrogen pick-up is similar to that obtained using technical nitrogen. Fig. 9 shows the corresponding mechanical properties. No large differences are observed between controlled and standard atmospheres. The higher impact strength of the uncontrolled argon sample and controlled nitrogen sample are attributed to their low oxygen content. The lower impact strength of the material produced with the nitrogen generator is believed to be associated to the higher oxygen content of the material. The obtained values are similar to that reported in the literature for 316 L stainless steel produced by L-PBF [1]. Still, in general the Charpy impact energy is close or even better than that of annealed wrought 316 L stainless steel (about 100 J) [22].

From Fig. 9 it also seems that there is no significant difference in tensile and yield strength between samples built in nitrogen and argon. If present, the strengthening effect of the nitrogen pick-up on the material properties depends on the quantity of nitrogen in solution and the presence and characteristics of nitrides (number, size, *etc.*). Still, only up to 50 ppm more nitrogen is picked up under nitrogen atmosphere in comparison to argon, with no strengthening noted, see Fig. 9. It is important to stress that all the values presented correspond to the material built with the fresh virgin powder. Regardless of the process atmosphere, the yield strength of the produced samples overpasses that of conventionally produced material. This may be explained by the fine microstructure of the material observed in Fig. 6. In Fig. 9, the ranges expected for the properties of conventionally produced material are indicated in light blue, according to the standards ASTM A240, ASTM A666 and ASTM A473. In the annealed state, 316 L stainless steel generally exhibits relatively low yield strength (*i.e.* about 200 MPa). Usually cold working results in the increase of the dislocation density and grain refinement, and thus in significant strengthening (ASTM A666). The specified properties for the 1/8 Hard state of 316 L stainless steel are quite similar to the L-PBF material ones (*i.e.* YS = 380 MPa, TS = 690 MPa, E = 25%).

The analysis of the fracture surface of the samples after impact test, produced under argon, highlights a ductile behaviour with small dimples. In some larger dimples, spherical oxides with the size of a few micrometres were observed, see Fig. 10. They were identified as being rich in Cr, Mn and Si by means of EDX. Similar observations can be made for samples built under nitrogen, see Fig. 11. The ductile fracture occurs by initiation, growth and coalescence of microvoids. The presence of inclusions causes voiding and promotes the ductile failure mechanisms. Since the oxygen pick-up difference between argon and nitrogen is only tens of ppm, it may be difficult to observe a difference in the volume fraction of these inclusions based on SEM observations. No nitrides were registered.

Fig. 12 displays the fracture surface of the impact samples produced with the internal nitrogen generator. In general, fine dimples are mostly observed on the fracture surface, indicating ductile failure of the

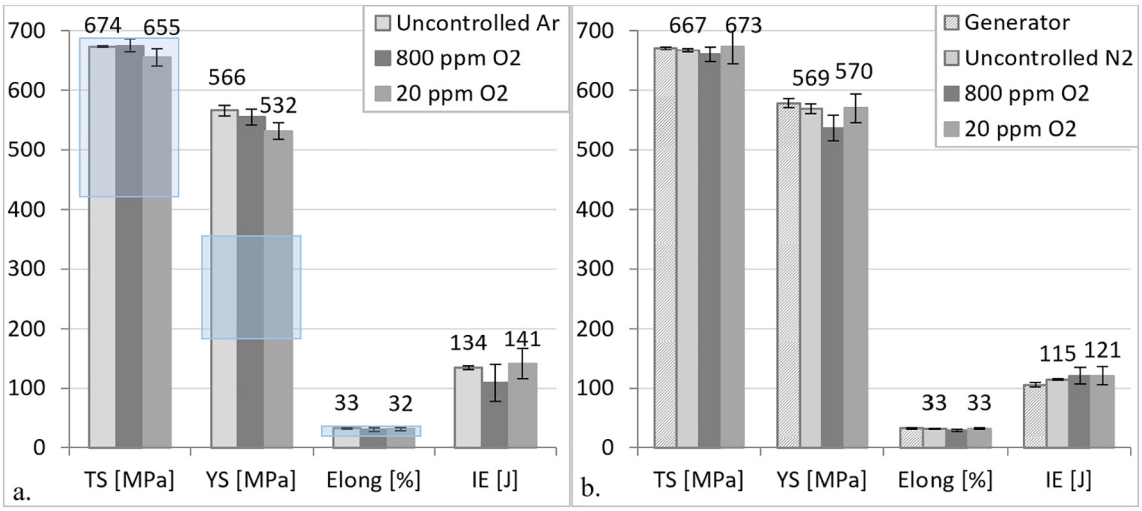

Fig. 9. Mechanical properties of parts built under a. argon and b. nitrogen.

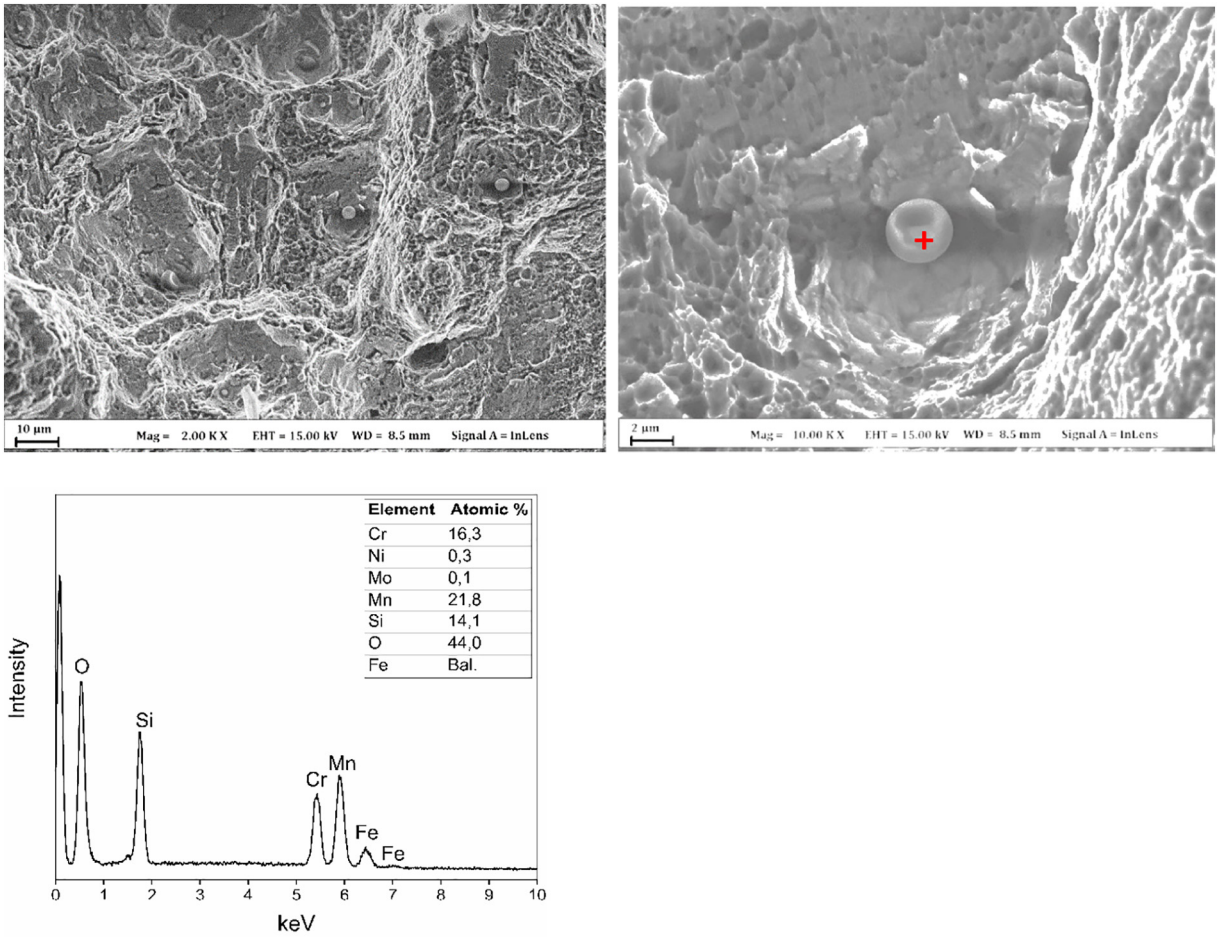

Fig. 10. SEM micrographs with EDX analysis of the fracture surface of the sample produced in argon after impact test.

material, as in case of other atmospheres, see Fig. 10 and Fig. 11. The significant difference of this sample is the presence of larger dimples, up to hundreds of micrometres in diameter, rather often observed on the fracture surface. They seem to be aligned along lines parallel to the building direction. These cavities are likely to have hosted larger spherical oxides or pores. They must belong to different build layers, revealed during impact testing. This pattern not being observed when processing under technical gas is consistent with the higher oxygen content and thus larger oxide formation.

3.4. Powder degradation

The SEM observations of powder samples highlighted degradation through the L-PBF process, see Figs. 13 to 15. Powder degradation is negligible in argon atmosphere and no effect after single processing in argon gas was observed. Processed under argon atmosphere and reused for 3 cycles, the powder rarely shows the presence of darker particulate features sizing below 1 µm. Those were also observed for the powder exposed to the nitrogen generator atmosphere. In addition, with the

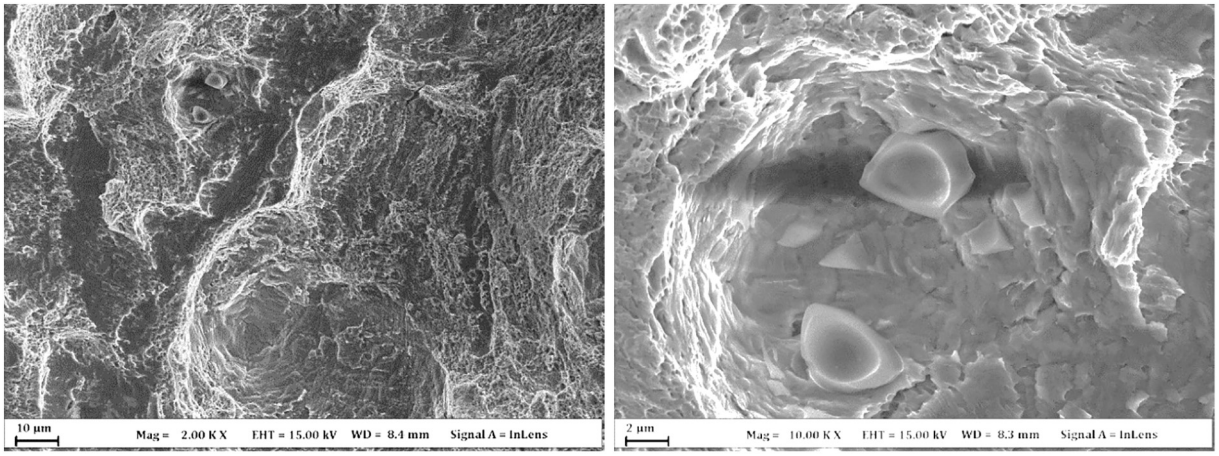

Fig. 11. SEM micrographs of the fracture surface of the sample produced in nitrogen after impact test.

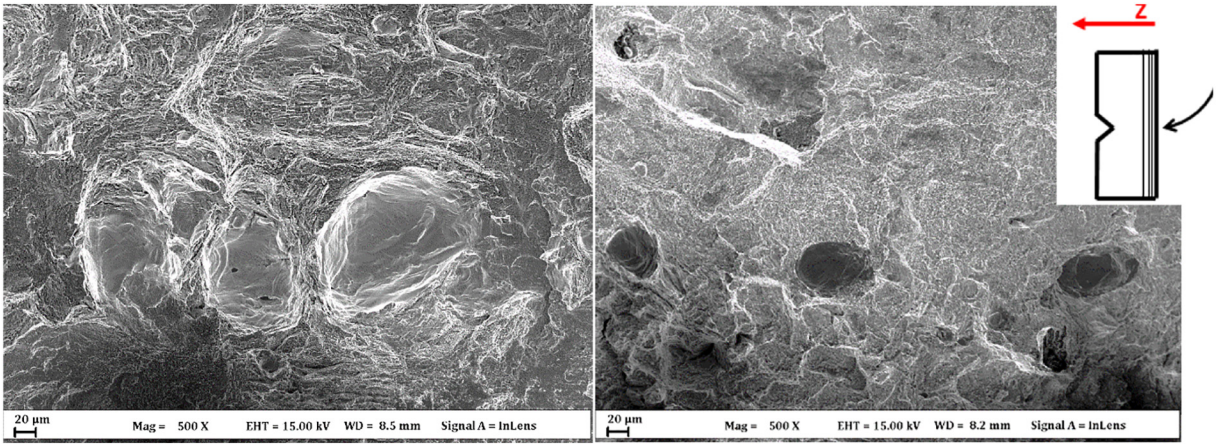

Fig. 12. SEM micrographs of the fracture surface of the sample produced with the internal nitrogen generator after impact test.

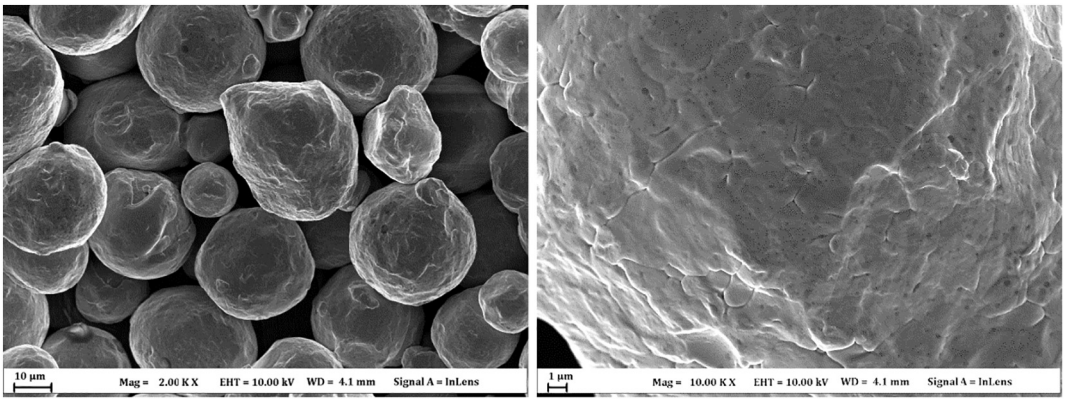

Fig. 13. SEM micrographs of the virgin powder.

nitrogen generator some particles showed a more critical oxidation with the presence of larger oxide features, covering significant area of the powder surface. The latter represent a fraction of the powder estimated to be less than 10% (from visual observation) already after one process cycle. As shown in Fig. 15, the typical size of the affected particle is clearly above 50 µm (here 57 µm), thus it remains after the sieving operation.

The L-PBF process is a relatively cold process that should not lead to the oxygen pick-up through the formation of the particulate oxide features as it requires substitutional diffusion of the alloying elements, sensitive to oxygen, to the powder surface. However, local overheating of the powder close to the build sample leads to an increase of temperature of the powder particles which promotes the mass transfer of elements with high affinity to oxygen from the bulk to the surface of the particle, for example Si, Cr and Mn for 316 L stainless steel. Small particle size results in the reduced diffusion path for alloying element – up to 25 µm for the particle of 50 µm in size. In combination with the high surface area, this explains the high reactivity and oxidation of the powder surface during the process. As observed in Fig. 14, dark particulates from a few nm up to 2 µm are observed. They are Cr-Mn oxides with traces of Si, based on EDX analysis. In Fig. 15, the presented particle is covered with larger but similar kind of particulates of up to 10 µm. With the

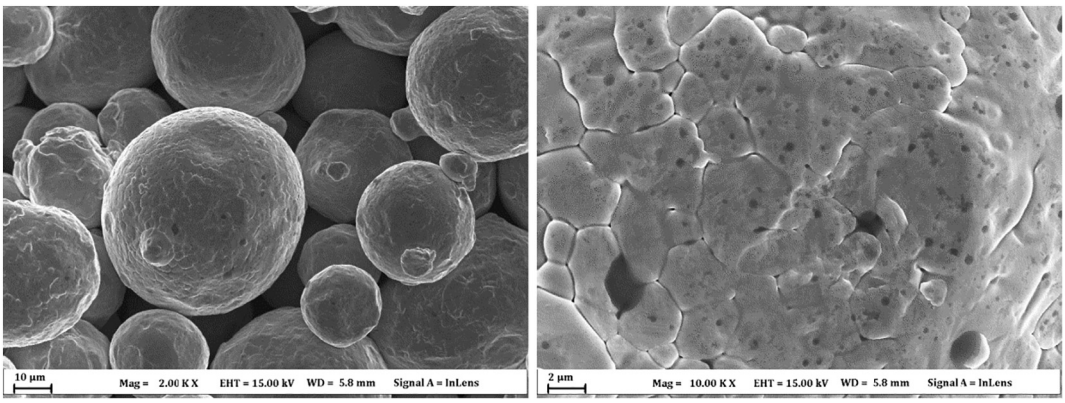

Fig. 14. SEM micrographs of the powder exposed to argon after three cycles.

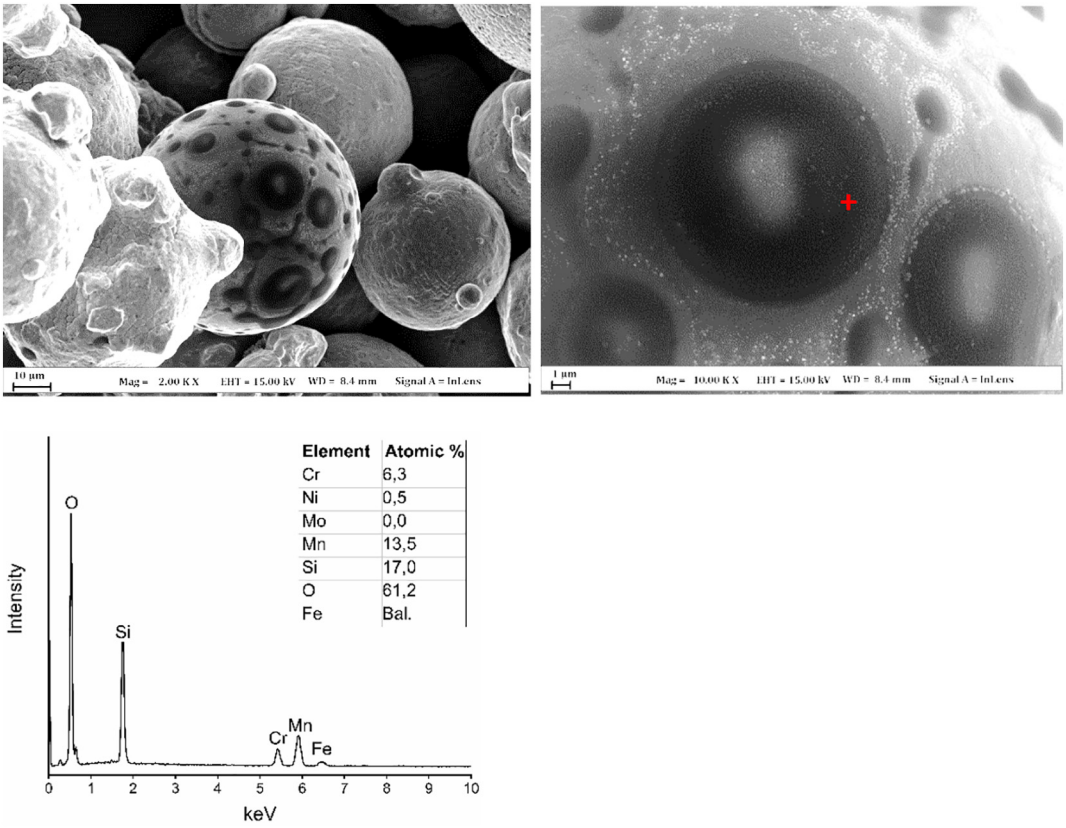

Fig. 15. SEM micrographs with EDX analysis of the powder exposed to the internal nitrogen generator after one cycle.

nitrogen generator, the temperature attained is not expected to vary a lot compared to argon processing, but the higher oxygen potential at the powder particle surface promotes the formation of these oxides and hence provides conditions for faster kinetics of powder oxidation.

Fig. 10 and Fig. 15 display the EDX spectra collected for the spherical oxide inclusions, typically observed on the fracture surfaces of the impact specimen produced in argon (see red cross in Fig. 10) and for the oxide features of the powder surface exposed to the atmosphere produced by the nitrogen generator (see red cross in Fig. 15). The qualitative compositions of the oxide particulates are presented in the corresponding tables. Similar results were obtained on the other fracture surfaces and on the features characterized by the dark contrast on the particle surface. The spherical oxide inclusions are typically submicrons sized and located in shallow dimples that do not allow proper qualitative analysis due to their fine size (smaller than the interaction volume during EDX) and result in the significant contribution from the surrounding metal matrix. However, the evident enrichment in Cr, Mn and Si indicates that the analysed features are thermodynamically stable oxide inclusions, see the Ellingham diagram in Fig. 16. The lower is the standard Gibbs free energy of formation of the oxide, the more stable the oxide can be expected. As demonstrated by Hryha et al. [23], oxide transformation in the case of Cr and Mn alloyed steels follows the thermodynamic stability of the possible oxides following sequence: $Fe_2O_3 \rightarrow FeO \rightarrow Fe_2MnO_4 \rightarrow Cr_2FeO_4 \rightarrow Cr_2O_3 \rightarrow MnCr_2O_4 \rightarrow MnO/MnSiO_x \rightarrow SiO_2$. To confirm the spinel structure of the observed oxide features, further TEM and APT investigations should be conducted.

Based on the close similarity and composition of the oxide inclusions observed on the fracture surface, with the composition and size of the oxide particulates observed on the powder surface, it can be assumed that the surface oxide state of the powder has a strong effect on the inclusions amount, distribution and composition in the L-PBF processed component. Oxide inclusions are likely to originate in the melt from the un-melted thermodynamically stable surface oxide features, inherited from the powder particle surface, that spheroidizes to minimize their surface energy and possibly also grew by agglomeration with other oxide inclusions. Hence, the rapid degradation of the powder particle surface during processing with the nitrogen generator atmosphere is assumed to be the reason for the large defects observed on the fracture surface of the impact specimens (see Fig. 15 and Fig. 12). Their shapes and size suggest that they are most probably lack-of-fusion defects connected to the secondary oxide phase, obtained during processing under atmosphere with the high oxygen potential.

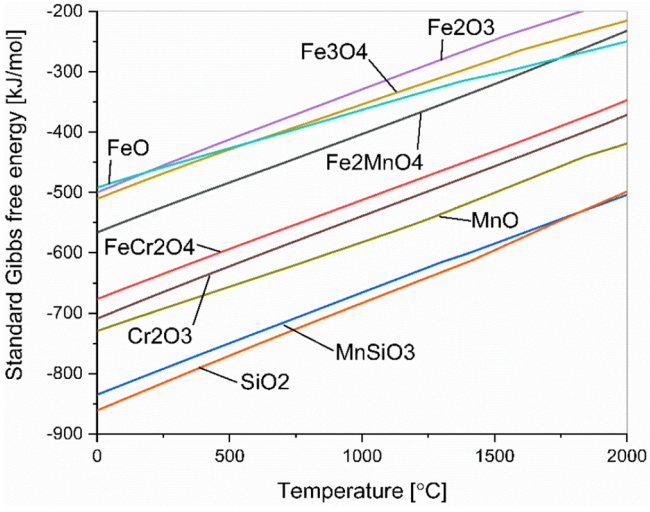

Fig. 16. Ellingham diagram for some possible oxides formed in the studied system (Plotted with HSC Chemistry).

4. Conclusions

The available gas supply solutions, limited to argon and nitrogen, result in different residual oxygen levels in the process atmosphere, depending on their initial purity and how the gas input is controlled. It has been shown that through external monitoring the amount of residual oxygen can be lowered to tens of ppm and kept stable during processing. Higher nitrogen dissolution was observed for all nitrogen atmospheres, regardless of the used gas purity. Similar oxygen content was obtained in parts produced under Argon 5.0 and Nitrogen 5.0. Processing under 800 ppm O_2 or 20 ppm O_2 did not affect the oxygen pick-up significantly in case of 316 L stainless steel. Still, the highest oxygen content was observed for the parts produced with the nitrogen generator (500 ppm O_2 and 750 ppm N_2), which is consistent with a higher oxygen partial pressure. The differences in oxygen and nitrogen dissolution appeared to have little effect on the mechanical properties, which are already overpassing that of conventionally processed 316 L stainless steel in terms of strength. Indeed, a yield strength of 566 $\pm$ 9 MPa and tensile strength of 674 $\pm$ 1 MPa are achieved using the standard argon atmosphere and a yield strength of 569 $\pm$ 8 MPa and tensile strength of 667 $\pm$ 3 MPa using nitrogen, for an elongation of 33 $\pm$ 1%. Difference in powder degradation even after one to three runs was though clearly seen in different atmospheres. Processing under high purity argon and nitrogen seems to have minor effect on powder and ensure robust L-PBF processing and excellent mechanical properties.

Data availability

The raw/processed data required to reproduce these findings cannot be shared at this time as the data also forms part of an ongoing study.

CRediT authorship contribution statement

Camille Pauzon: Conceptualization, Formal analysis, Investigation, Writing - original draft, Writing - review & editing. **Eduard Hryha:** Supervision, Formal analysis, Writing - original draft. **Pierre Forêt:** Methodology, Resources, Writing - original draft. **Lars Nyborg:** Conceptualization, Writing - original draft.

Acknowledgments

The work was performed in the framework of the Centre for Additive Manufacturing – Metal (CAM^2), supported by Vinnova. The authors would like to acknowledge the technical support from Höganäs AB for material testing.

References

[1] Y. Zhong, L. Liu, S. Wikman, D. Cui, Z. Shen, Intragranular cellular segregation network structure strengthening 316L stainless steel prepared by selective laser melting, J. Nucl. Mater. 470 (2016) 170–178, https://doi.org/10.1016/j.jnucmat.2015.12.034.
[2] A. Leicht, U. Klement, E. Hryha, Effect of build geometry on the microstructural development of 316L parts produced by additive manufacturing, Mater. Charact. 143 (2018) 137–143, https://doi.org/10.1016/j.matchar.2018.04.040.
[3] Y.M. Wang, T. Voisin, J.T. Mckeown, J. Ye, N.P. Calta, Z. Li, Z. Zeng, Y. Zhang, W. Chen, T.T. Roehling, R.T. Ott, M.K. Santala, P.J. Depond, M.J. Matthews, A.V. Hamza, T. Zhu, Additively manufactured hierarchical stainless steels with high strength nd ductility, Nat. Mater. 17 (2018)https://doi.org/10.1038/NMAT5021.
[4] R. Casati, J. Lemke, M. Vedani, Microstructure and fracture behavior of 316L austenitic stainless steel produced by selective laser melting, J. Mater. Sci. Technol. 32 (2016) 738–744, https://doi.org/10.1016/j.jmst.2016.06.016.
[5] J.A. Cherry, H.M. Davies, S. Mehmood, N.P. Lavery, S.G.R. Brown, J. Sienz, Investigation into the effect of process parameters on microstructural and physical properties of 316L stainless steel parts by selective laser melting, Int. J. Adv. Manuf. Technol. 76 (2014) 869–879, https://doi.org/10.1007/s00170-014-6297-2.
[6] Z. Sun, X. Tan, S.B. Tor, W.Y. Yeong, Selective laser melting of stainless steel 316L with low porosity and high build rates, Mater. Des. 104 (2016) 197–204, https://doi.org/10.1016/j.matdes.2016.05.035.
[7] A. Riemer, S. Leuders, M. Thöne, H.A. Richard, T. Tröster, T. Niendorf, On the fatigue crack growth behavior in 316L stainless steel manufactured by selective laser melting, Eng. Fract. Mech. 120 (2014) 15–25, https://doi.org/10.1016/j.engfracmech.2014.03.008.
[8] Renishaw, n.d. Our Technology [WWW Document]. URL http://www.renishaw.com/en/our-technology–27362 (accessed 3.28.18).
[9] M.J. Matthews, G. Guss, S.A. Khairallah, A.M. Rubenchik, P.J. Depond, W.E. King, Acta Materialia denudation of metal powder layers in laser powder bed fusion processes, Acta Mater. 114 (2016) 33–42, https://doi.org/10.1016/j.actamat.2016.05.017.
[10] S.A. Khairallah, A.T. Anderson, A. Rubenchik, W.E. King, Laser powder-bed fusion additive manufacturing: physics of complex melt flow and formation mechanisms of pores, spatter, and denudation zones, Acta Mater. 108 (2016) 36–45, https://doi.org/10.1016/j.actamat.2016.02.014.
[11] A. Masmoudi, R. Bolot, C. Coddet, Investigation of the laser-powder-atmosphere interaction zone during the selective laser melting process, J. Mater. Process. Technol. 225 (2015) 122–132, https://doi.org/10.1016/j.jmatprotec.2015.05.008.
[12] D. Dai, D. Gu, Effect of metal vaporization behavior on keyhole-mode surface morphology of selective laser melted composites using different protective atmospheres, Appl. Surf. Sci. 355 (2015) 310–319, https://doi.org/10.1016/j.apsusc.2015.07.044.
[13] M. Aden, E. Beyer, G. Herziger, Laser-induced vaporisation of metal as a Riemann problem, J. Phys. D. Appl. Phys. 23 (1990) 655–661, https://doi.org/10.1088/0022-3727/23/6/004.
[14] S. Ly, A.M. Rubenchik, S.A. Khairallah, G. Guss, M.J. Matthews, Metal vapor micro-jet controls material redistribution in laser powder bed fusion additive manufacturing, Sci. Rep. 7 (2017) 1–12, https://doi.org/10.1038/s41598-017-04237-z.
[15] A. Ladewig, G. Schlick, M. Fisser, V. Schulze, U. Glatzel, Influence of the shielding gas flow on the removal of process by-products in the selective laser melting process, Addit. Manuf. 10 (1–9) (2016)https://doi.org/10.1016/j.addma.2016.01.004.
[16] R. Li, J. Liu, Y. Shi, L. Wang, W. Jiang, Balling behavior of stainless steel and nickel powder during selective laser melting process, Int. J. Adv. Manuf. Technol. 59 (2012) 1025–1035, https://doi.org/10.1007/s00170-011-3566-1.
[17] B. Ferrar, L. Mullen, E. Jones, R. Stamp, C.J. Sutcliffe, Gas flow effects on selective laser melting (SLM) manufacturing performance, J. Mater. Process. Technol. 212 (2012) 355–364, https://doi.org/10.1016/j.jmatprotec.2011.09.020.
[18] P. Bidare, I. Bitharas, R.M. Ward, M.M. Attallah, A.J. Moore, Fluid and particle dynamics in laser powder bed fusion, Acta Mater. 142 (2018) 107–120, https://doi.org/10.1016/j.actamat.2017.09.051.
[19] M. Schniedenharn, J.H. Schleifenbaum, On the Correlation of the Shielding Gas Flow in L-PBF Machines With Part Densit, 2018 1–7.
[20] P.A. Kuznetsov, A.A. Zisman, S.N. Petrov, I.S. Goncharov, Structure and mechanical properties of austenitic 316L steel produced by selective laser melting, Metally 2016 (2016) 930–934, https://doi.org/10.1134/S0036029516100104.
[21] J.R. Trelewicz, G.P. Halada, O.K. Donaldson, G. Manogharan, Microstructure and corrosion resistance of laser additively manufactured 316L stainless steel, Jom 68 (2016) 850–859, https://doi.org/10.1007/s11837-016-1822-4.
[22] P.D. Harvey, Stainless and heat-resisting steels, Engineering Properties of Steel, 1982.
[23] E. Hryha, E. Dudrova, L. Nyborg, On-line control of processing atmospheres for proper sintering of oxidation-sensitive PM steels, J. Mater. Process. Technol. 212 (2012) 977–987, https://doi.org/10.1016/j.jmatprotec.2011.12.008.